Available online at www.sciencedirect.com
SCIENCE DIRECT®
Journal of Computational Physics 203 (2005) 176–190
JOURNAL OF COMPUTATIONAL PHYSICS
www.elsevier.com/locate/jcp

A new multistack radiation boundary condition for FDTD based on self-teleportation of fields

Rodolfo E. Diaz, Igor Scherbatko *

Material-Wave Interaction Laboratory, Electrical Engineering Department, Arizona State University, Tempe Center, 951 S. Mill Ave., Suite # 199, Tempe, AZ 85287-9509, USA

Received 10 December 2003; received in revised form 20 July 2004; accepted 12 August 2004
Available online 6 October 2004

Abstract

In [Electromagnetics 23 (2003) 187], a technique for injecting perfect plane waves into finite regions of space in FDTD was reported. The essence of the technique, called Field Teleportation, is to invoke the principle of equivalent sources using FDTDs discrete definition of the curl to copy any field propagating in one FDTD domain to a finite region of another domain. In this paper, we apply this technique of Field Teleportation to the original domain itself to create a transparent boundary across which any outward traveling FDTD field produces an exact negative copy of itself. When this copied field is teleported one cell ahead and one cell forward in time it causes significant self-cancelation of the original field. Illustrative experiments in two-dimensions show that a two-layer (10-cell thick) multi-stack Radiation Boundary Condition (RBC) with a simplest Huygens's termination readily yields reflection coefficients of the order of −80 dB up to grazing incidence for all the fields radiated by a harmonic point source ($\lambda = 30$ cells) in free space located 20 cells away from the boundary. Similarly low levels of artificial reflection are demonstrated for a case in which the RBC cuts through five different magnetodielectric materials.
© 2004 Elsevier Inc. All rights reserved.

Keywords: FDTD; Radiation boundary conditions

1. Introduction

Traditional Radiation Boundary Conditions (RBCs) for FDTD consist of algorithms for extrapolation of the internal spatial-time field distribution into the boundary of the computational grid (enclosing the grid). The two most popular techniques for implementing an RBC are mode-annihilating and one-way

* Corresponding author. Tel.: +1 480 965 3274; fax: +1 480 965 3148.
E-mail address: igor_s@asu.edu (I. Scherbatko).

0021-9991/$ - see front matter © 2004 Elsevier Inc. All rights reserved.
doi:10.1016/j.jcp.2004.08.011

wave equation approximations. Both approaches are based on differential equations providing a local approximation of the radiation properties that are inherent to Maxwell's equations [2].

The RBCs most often referred to in the literature are those proposed by Engquist and Majda [3] with the discretization derived by Mur [4]. These are based on an approximation of the outgoing wave equation by linear expressions using either a Taylor or a Pade approximation. In the RBC proposed by Higdon a linear superposition of plane waves has been considered for derivation of an exact annihilator operator at each of the pre-selected incident angles [5]. An alternative approach has been followed by Fang and Mei [6], who use RBCs to estimate both E and H field at a point on the boundary and then combine the results in such a way as to improve the overall accuracy. The technique has been referred to as the Super Absorbing Correction. Deveze et al. [7] also use a combination of the E and H field arranged in a special way to reduce the order of the derivatives that need to be evaluated.

Historically, RBC methods were very popular until the Perfect Matched Layer (PML) was proposed by Berenger [8]. Since then, FDTD practitioners have concluded that superior field absorption can be achieved by introduction of gradually absorptive materials rather than one-cell RBCs. The PML was derived initially as a multi-cell absorption layer capable of absorbing outgoing waves in a wide range of incident angles. However, implementing a PML is not a trivial undertaking, especially for the material intersections and terminations.

Despite the popularity of the PML, efforts in RBC improvement and the quest for the best absorption boundary condition continues. For example, Liao et al. [9] reported the superiority of their RBC based on the measured equation on invariance in time domain (TDMEI) over the PML in a two-dimensional implementation. However, the TDMEI approach, based on storing a spatial-time history of the fields close to the boundary up to seven time steps in the past, has quite a high computational cost [10].

Ergin et al. [11] presented their plane-wave time-domain scheme as an enhanced global exact RBC method and reported results comparable to eight layer PML. Recently, a hybrid one-way Sommerfeld-PML scheme has been proposed by Vay combining the flexibility of the PML and the simplicity of one-way wave RBC [12]. However, the late-time performance of this scheme (stability) has not been reported yet.

Recently, a new re-radiating boundary condition for terminating the FDTD grid has been reported in [13] based on the discrete version of Schelkunoff's equivalent currents (or so-called Field Teleportation Technique). In this paper, we detail the derivation of the approach and demonstrate its capabilities through illustrative numerical experiments. The Field Teleportation Technique was used in [1] to teleport perfect plane waves into finite regions of FDTD with no leakage. Here, the RBC effect is obtained by teleporting outgoing fields back into the FDTD domain with a negative sign, thus partially canceling outward traveling waves.

Section 2 of this paper introduces a theory of discrete equivalent currents and shows how they can be included in the regular FDTD update procedure and thus allows the teleportation of fields. Section 3 presents a recipe for RBC update inside the FDTD time-marching algorithm. In Section 4, the Field Teleportation scheme is implemented within the source grid to create the multistack RBC (MS-RBC). After comparing this technique with the standard PML in free space, we demonstrate its excellent performance by terminating a domain with an inhomogeneous boundary between multiple regions of lossless and lossy dielectrics.

2. Self-teleportation of fields

The surface equivalence theorem primarily introduced in 1936 by Schelkunoff plays an important role in electromagnetic theory and applications. Modeling of electromagnetic scattering, diffraction and aperture antenna problems are common examples of the theorem's applications. According to the theorem, the field

outside a source region surrounded by an imaginary closed surface S can be obtained by introduction, over this surface, of equivalent tangential electric $\vec{K}_e$ and magnetic $\vec{K}_m$ current densities (sometimes called Schelkunoff's currents) [14]. The current densities are selected so that the fields inside the closed surface are zero and outside are equal to the total field. These currents are related to the tangential fields on the surface S by the following expressions:

$$\vec{K}_e = \hat{n} \times \vec{H}_{tot}, \quad \vec{K}_m = -\hat{n} \times \vec{E}_{tot}, \tag{1}$$

where $\hat{n}$ is the outward surface normal to S. These equivalent currents constitute an impressed one-sided source, that cancels its own fields inside the enclosed surface and produces outside an exact replica of the original fields. Clearly, by reversing the sign of the impressed currents their self-canceling property inside S is unaffected but now they produce outside S the negative of the original fields. Therefore, if these outside fields were added to the original fields there would be destructive interference everywhere outside. This is an ideal situation for an FDTD boundary condition.

Fig. 1 demonstrates an example of the FDTD Field Teleportation method for a two-dimensional rectangular area, which is excited by a TE line source located at $x = 50$, $y = 50$ cell. A smooth bipolar pulse is injected and the EM field propagates as a free cylindrical wave during the first 100 time steps. (For this simulation $dx = dy = ds$, $dt = ds/2c$). The Field Teleportation technique has been used to generate an exact negative replica of the outgoing wave measured at the plane $x = 75$ (measurement plane) and teleported 25 cells to the right (teleportation plane). The utilized algorithm creates strictly a one-sided wave (backward leakage is negligible, less than -300 dB [1]) with opposite polarity to the original wave.

Since discrete equivalent currents are applied to create a soft one-sided source, the teleportation boundary is transparent to waves from any direction (It does not affect any signal propagating through it). If we move the teleportation plane towards the measurement one, the interference between the original and teleported wave becomes more destructive (in the ideal case causing total suppression of the outgoing signal when the planes coincide).

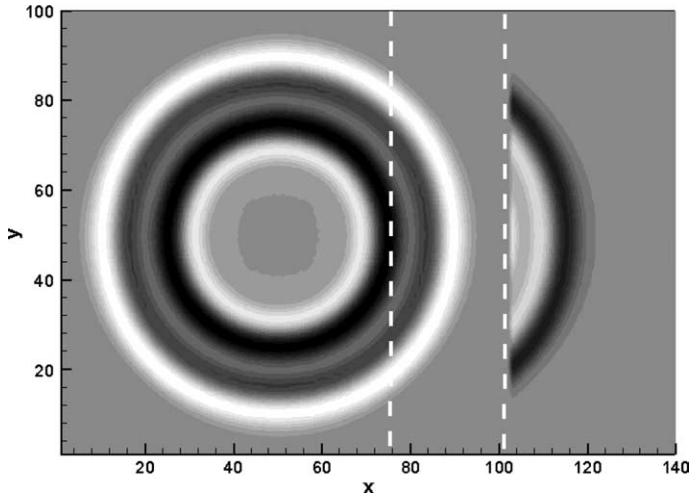

Fig. 1. Example of the Field Teleportation of the cylindrical wave. The measurement plane is located at $x = 75$, the teleportation plane is at ($x = 100$). An exact negative copy of the original wave is generated.

The attainment of perfect cancellation forwards would then depend on exact spatio-temporal coincidence of the original field and the teleported copy. Thus the RBC can be implemented using the discrete version of Schelkunoff's equivalent currents.

Let us consider a simple dispersive medium with permittivity $\varepsilon = \varepsilon_0\varepsilon_r$, permeability $\mu = \mu_0\mu_r$, electric and magnetic conductivities σ_e and σ_m, respectively. The Maxwell's equations for the sourceless case have the form:

$$\mu\frac{\partial\vec{H}}{\partial t} + \sigma_m\vec{H} = -\vec{\nabla}\times\vec{E}, \tag{2a}$$

$$\varepsilon\frac{\partial\vec{E}}{\partial t} + \sigma_e\vec{E} = \vec{\nabla}\times\vec{H}. \tag{2b}$$

Let us suppose we have additional current sources, which are impressed electric $\vec{J}_e$ and magnetic $\vec{J}_m$ currents. Then these impressed currents must enter into the right-hand sides of the curl equation as follows:

$$\mu\frac{\partial\vec{H}}{\partial t} + \sigma_m\vec{H} = -\vec{\nabla}\times\vec{E} - \vec{J}_m, \tag{3a}$$

$$\varepsilon\frac{\partial\vec{E}}{\partial t} + \sigma_e\vec{E} = \vec{\nabla}\times\vec{H} - \vec{J}_e. \tag{3b}$$

These equations being discretized in time by the classical FDTD scheme lead to following update expressions:

$$\left(\vec{H}^{n+1/2} - \vec{H}^{n-1/2}\right) + \frac{\sigma_m\Delta t}{2\mu}\left(\vec{H}^{n+1/2} + \vec{H}^{n-1/2}\right) = -\frac{\Delta t}{\mu}\left(\vec{\nabla}\times\vec{E}^{n}\right) - \frac{\Delta t}{\mu}\vec{J}_m, \tag{4a}$$

$$(\vec{E}^{n+1} - \vec{E}^{n}) + \frac{\sigma_e\Delta t}{2\varepsilon}(\vec{E}^{n+1} + \vec{E}^{n}) = \frac{\Delta t}{\varepsilon}\left(\vec{\nabla}\times\vec{H}^{n+1/2}\right) - \frac{\Delta t}{\varepsilon}\vec{J}_e, \tag{4b}$$

where the upper index indicates the FDTD time step. Recognizing that in the discrete space of FDTD, $\vec{J}_e = \vec{K}_e/ds, \vec{J}_m = \vec{K}_m/ds$, with ds being the size of the space cell, then substitution of J_e and J_m into (4a) and (4b) gives

$$(\vec{H}^{n+1/2} - \vec{H}^{n-1/2}) + \frac{\sigma_m\Delta t}{2\mu}(\vec{H}^{n+1/2} + \vec{H}^{n-1/2}) = -\frac{\Delta t}{\mu}\left(\vec{\nabla}\times\vec{E}^{n}\right) - \frac{\Delta t}{\mu ds}\vec{K}_m, \tag{5a}$$

$$(\vec{E}^{n+1} - \vec{E}^{n}) + \frac{\sigma_e\Delta t}{2\varepsilon}(\vec{E}^{n+1} + \vec{E}^{n}) = \frac{\Delta t}{\varepsilon}\left(\vec{\nabla}\times\vec{H}^{n+\frac{1}{2}}\right) - \frac{\Delta t}{\varepsilon ds}\vec{K}_e. \tag{5b}$$

Eqs. (5) after simplifications take the form:

$$\vec{H}^{n+1/2} = \frac{1 - \frac{\sigma_m\Delta t}{2\mu}}{1 + \frac{\sigma_m\Delta t}{2\mu}}\vec{H}^{n-1/2} - \frac{\Delta t}{(\mu + \sigma_m\Delta t/2)}\left(\vec{\nabla}\times\vec{E}^{n}\right) - \frac{\Delta t}{ds(\mu + \sigma_m\Delta t/2)}\vec{K}_m, \tag{6a}$$

$$\vec{E}^{n+1} = \frac{1 - \frac{\sigma_e\Delta t}{2\varepsilon}}{1 + \frac{\sigma_e\Delta t}{2\varepsilon}}\vec{E}^{n} + \frac{\Delta t}{(\varepsilon + \sigma_e\Delta t/2)}\left(\vec{\nabla}\times\vec{H}^{n+\frac{1}{2}}\right) - \frac{\Delta t}{ds(\varepsilon + \sigma_e\Delta t/2)}\vec{K}_e. \tag{6b}$$

Expressions (6a) and (6b) differ from the conventional FDTD scheme only by the additional rightmost terms and therefore can be implemented into the FDTD algorithm easily.

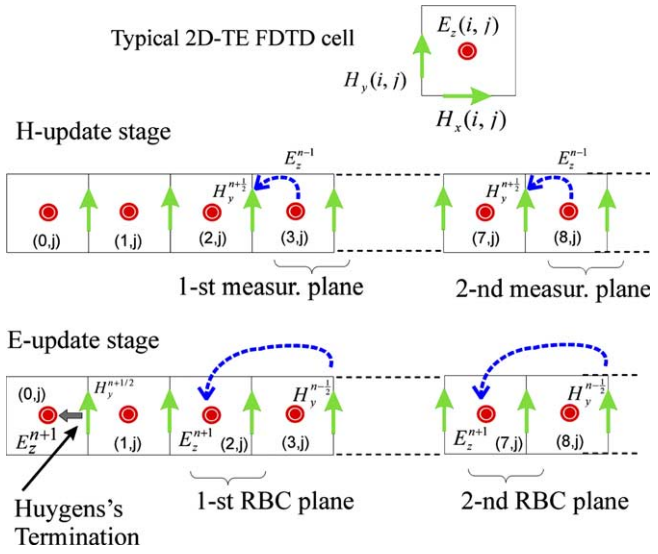

Fig. 2. Double RBC field termination implemented on the left side of the 2D domain, after H- and E-update loops.

3. RBC-Updating scheme

In the proposed FDTD computer program, the implementation would be as follows. For the sake of simplicity only the case of a 2D-space is given with the three field components E_z, H_x and H_y being considered. (This is the case where the electric field is transverse to the plane of incidence, or TE case). The 2D grid is an array with index i varying from 0 to $nx + 1$ in the x-direction, index j is changing from 0 to $ny + 1$ in the y-direction. Fig. 2 shows the FDTD cell with our indexing convention and terminating on the left side in an RBC. The tangential field components $E_z(3, j)$ and $H_y(4, j)$ define the outermost measurement plane whereas $E_z(2, j)$ and $H_y(3, j)$ constitute the corresponding teleportation plane (that is, the RBC plane). Note, that the RBC plane is not coincident with the teleportation plane to avoid feedback instabilities. A second RBC plane is separated from the first one by three cells to the right. A final Huygens's termination (explained below, see Eqs. (14) and (15)) is placed exactly at the left edge of the domain. Table 1 presents the locations of the outermost RBC planes on the entire 2D domain, placed symmetrically with respect to the center of the domain.

The time-loop ($n = 0, \ldots, nt$) starts with source field injection, followed by H_x- and H_y updating nested loops. The FDTD algorithm then updates the magnetic fields according to the curl-equations:

$$H_x^{n+1/2}(i,j) = C_{ma}(i,j)H_x^{n-1/2}(i,j) - C_{mb}(i,j)(E_z^n(i,j) - E_z^n(i,j-1)), \quad i = 1,\ldots,nx, \;\; j = 1, ny+1, \tag{7}$$

Table 1
Locations of the second RBC walls

	H-update RBC loops	E-update RBC loops
Left wall	$H_y(8, j)$, $j = 1, \ldots, ny$	$E_z(7, j)$, $j = 1, \ldots, ny$
Right wall	$H_y(nx - 5, j)$, $j = 1, \ldots, ny$	$E_z(nx - 5, j)$, $j = 1, \ldots, ny$
Top wall	$H_x(i, ny - 5)$, $i = 1, \ldots, nx$	$E_z(i, ny - 5)$, $i = 1, \ldots, nx$
Bottom wall	$H_x(i, 8)$, $i = 1, \ldots, nx$	$E_z(i, 7)$, $i = 1, \ldots, nx$

$$H_y^{n+1/2}(i,j) = C_{ma}(i,j)H_y^{n-1/2}(i,j) + C_{mb}(i,j)(E_z^n(i,j) - E_z^n(i-1,j)), \quad i = 1,\ldots,nx+1, \;\; j = 1,ny, \tag{8}$$

where

$$C_{ma}(i,j) = \left(1 - \frac{\sigma_m(i,j)\Delta t}{2\mu(i,j)}\right) \Big/ \left(1 + \frac{\sigma_m(i,j)\Delta t}{2\mu(i,j)}\right) \quad \text{and} \quad C_{mb}(i,j) = \left(\frac{\Delta t}{\mu(i,j)ds}\right) \Big/ \left(1 + \frac{\sigma_m(i,j)\Delta t}{2\mu(i,j)}\right).$$

Now we update the tangential magnetic field on the RBC-planes at the same time step ($T = n + 1/2$). Fig. 2 (at the H-update stage) schematically shows the procedure for the left boundary. On the left and right external RBC planes for all H_y-components inside the j-loop we have:

$$\begin{cases} H_y^{n+1/2}(3,j) = H_y^{n+1/2}(3,j) - A_{hl}(j)E_z^{n-1}(3,j), \quad j = 1,\ldots,ny, \\ H_y^{n+1/2}(nx-1,j) = H_y^{n+1/2}(nx-1,j) + A_{hr}(j)E_z^{n-1}(nx-2,j), \quad j = 1,\ldots,ny, \end{cases} \tag{9}$$

where

$$A_{hl}(j) = \frac{R\Delta t}{ds(\mu(3,j) + \sigma_m(3,j)\Delta t/2)}, \quad A_{hr}(j) = \frac{R\Delta t}{ds(\mu(nx-1,j) + \sigma_m(nx-1,j)\Delta t/2)}$$

and R is a damping factor introduced for a stability reasons (discussed below). Note, that impressed currents have been introduced as the negative copies (with the opposite sign) to the Schelkunoff's equivalent currents to cancel the outgoing waves. Since we measure the incident field one half-step ahead of the RBC-wall, we have to take into account a time delay. Therefore, we use the delayed value E_z^{n-1} (electric field at one time-step back). This assumption works perfectly for $ds/c\Delta t = 0.5$ ratio (c is the speed of light in the medium).

Of necessity the permittivity and conductivity associated with the two neighboring cells (where we measure the field and where we introduce the impressed currents) must be the same. That means that there is no variation of the material parameters perpendicular to the plane, within two cells. However, this algorithm allows arbitrary transverse variation of the material (along the wall). The bottom and top external RBC planes are updated in the i-loop by the following equations:

$$\begin{cases} H_x^{n+1/2}(i,3) = H_x^{n+1/2}(i,3) + A_{hb}(i)E_z^{n-1}(i,3), \quad i = 1,\ldots,nx, \\ H_x^{n+1/2}(i,ny-1) = H_x^{n+1/2}(i,ny-1) - A_{ht}(i)E_z^{n-1}(i,ny-2), \quad i = 1,\ldots,nx, \end{cases} \tag{10}$$

where

$$A_{hb}(i) = \frac{R\Delta t}{ds(\mu(i,3) + \sigma_m(i,3)\Delta t/2)} \text{ and } A_{ht}(i) = \frac{R\Delta t}{ds(\mu(i,ny-1) + \sigma_m(i,ny-1)\Delta t/2)}.$$

Late-time stability is a common problem for many RBCs and introduction of a damping factor is a usual practice. The R coefficient ensures late-time stability of the proposed algorithm. This safety measure is motivated by the fact that the impressed currents create energy, and truncation noise can therefore lead the planes to create noise energy. In all numerical experiments performed to date decreasing the magnitude of the impressed currents by 1% (or letting $R = 0.99$) is sufficient to ensure stability [13]. The reason such a slight damping works is that the built in spatio-temporal delay in the recipe does not create a symmetric boundary in FDTD. From the front side the RBC is an absorber and differentiator, from the back side it is an imperfect integrator. As shown in [13], the combination of the RBC absorption (and differentiating property) with the further absorption (and differentiation) at the Huygens's termination results in an echo that cannot be reconstructed on the way back through the RBC.

After the RBC updating step, we return to the conventional FDTD scheme. The E_z-component of the electromagnetic field is updated next by the following expression, inside two nested loops:

$$E_z^{n+1}(i,j) = C_{ea}(i,j)E_z^n(i,j) + C_{eb}(i,j)\text{curl } H, \quad i = 1,\ldots,nx, \;\; j = 1,\ldots,ny, \tag{11}$$

where

$$\text{curl } H = H_x^{n+1/2}(i,j) + H_y^{n+1/2}(i+1,j) - H_x^{n+1/2}(i,j+1) - H_y^{n+1/2}(i,j),$$

$$C_{ea}(i,j) = \left(1 - \frac{\sigma_e(i,j)\Delta t}{2\varepsilon(i,j)}\right) \Big/ \left(1 + \frac{\sigma_e(i,j)\Delta t}{2\varepsilon(i,j)}\right) \quad \text{and} \quad C_{eb}(i,j) = \left(\frac{\Delta t}{\varepsilon(i,j)ds}\right) \Big/ \left(1 + \frac{\sigma_e(i,j)\Delta t}{2\varepsilon(i,j)}\right).$$

Right after the E_z updating part, the RBC E_z-updating loop follows (schematically shown in Fig. 2 as E-update stage).

Let us consider the left-side termination again. The one time-step delayed H_y-component is transformed into an impressed current and added to the E_z field component. Therefore, the updating equations for the left and right external RBC planes are:

$$\begin{cases} E_z^{n+1}(2,j) = E_z^{n+1}(2,j) - A_{\text{el}}(j)H_y^{n-1/2}(4,j), \quad j = 1,\ldots,ny, \\ E_z^{n+1}(nx-1,j) = E_z^{n+1}(nx-1,j) + A_{\text{er}}(j)H_y^{n-1/2}(nx-2,j), \quad j = 1,\ldots,ny, \end{cases} \tag{12}$$

where

$$A_{\text{el}}(j) = \frac{R\Delta t}{ds(\varepsilon(2,j) + \sigma_{\text{e}}(2,j)\Delta t/2)} \text{ and } A_{\text{er}}(j) = \frac{R\Delta t}{ds(\varepsilon(nx-1,j) + \sigma_e(nx-1,j)\Delta t/2)}.$$

Here the parameter R is the same as in the previous case. Similarly, the update equations for the top and bottom external RBC planes are as follows:

$$\begin{cases} E_z^{n+1}(i,ny-1) = E_z^{n+1}(i,ny-1) - A_{\text{et}}(i)H_x^{n-1/2}(i,ny-2), \quad i = 1,\ldots,nx, \\ E_z^{n+1}(i,2) = E_z^{n+1}(i,2) + A_{eb}(i)H_x^{n-1/2}(i,4), \quad i = 1,\ldots,nx, \end{cases} \tag{13}$$

where

$$A_{\text{et}}(i) = \frac{R\Delta t}{ds(\varepsilon(i,ny-1) + \sigma_{\text{e}}(i,ny-1)\Delta t/2)} \quad \text{and} \quad A_{\text{eb}}(i) = \frac{R\Delta t}{ds(\varepsilon(i,4) + \sigma_{\text{e}}(i,4)\Delta t/2)}.$$

Strictly speaking, we have not terminated the E_z-field completely but just suppressed it substantially. The E_z fields at the edges of the domain have not been updated yet. In fact they are not updated in the ordinary sense but rather are used to implement a very simple domain termination we call the Huygens's termination. This termination simply gives these E_z fields at every time step the value required to mimic an outgoing normal incidence plane, wave given the value of the tangential H-field immediately inside the boundary. Thus for these fields we assume $E = \eta H$, where η is the characteristic impedance of the media. Using the time-domain analogue of the well-known expression for the complex permittivity and permeability in frequency domain, we will have:

$$\begin{cases} E_z^{n+1}(0,j) = \eta(0,j)H_y^{n+1/2}(1,j), \quad j = 1,\ldots,ny, \\ E_z^{n+1}(nx+1,j) = -\eta(nx+1,j)H_y^{n+1/2}(nx+1,j), \quad j = 1,\ldots,ny \end{cases} \tag{14}$$

and for the top and bottom termination correspondingly:

$$\begin{cases} E_z^{n+1}(i,ny+1) = \eta(i,ny+1)H_x^{n+1/2}(i,ny+1), \quad i = 1,\ldots,nx, \\ E_z^{n+1}(i,0) = -\eta(i,1)H_x^{n+1/2}(i,1), \quad i = 1,\ldots,nx, \end{cases} \tag{15}$$

where

$$\eta(i,j) = \sqrt{\frac{\mu(i,j) + \sigma_m(i,j)\Delta t}{\varepsilon(i,j) + \sigma_e(i,j)\Delta t}}.$$

As it has been mentioned before, due to the small phase and magnitude mismatch between the original and the teleported field, only one RBC plane does not suppress the outgoing field completely, there is always some transmission through the boundary. The remainder looks like a dim version of its first time derivative. Original results reported in [13] show that a pulse encountering the RBC teleportation boundary from the wrong side would be expected to undergo re-integration but in strange way, since portions of the pulse that have crossed the boundary find themselves teleported back behind where they first entered the boundary, actually creating excess energy. If we did not have the one-time-step delay buffer in the recipe, this would constitute a fatal flaw in the RBC. That delay reduces this backwards interaction to a mild re-integration of the pulse. As it has been shown in [13], the biggest problem with pulses entering the proposed RBC boundary from the wrong side is their dc content. Fortunately, on the way forward, the differentiating property of the RBC strips off most of the dc content of all signals.

A stack of RBC-walls can be employed to get better absorption. Two or three RBC planes give a reasonable absorption for many practical applications. We have found that two neighbor RBC planes should be separated by at least two cells. However, at this distance the two walls are coupled through the curl so that for maximum late-time stability we recommend a three-cell separation. In our modeling, we use two RBC-walls plus the Huygens's termination that result in a 10 cells absorption layer on each side. (This is counting the teleportation source cells and the last cell in the domain as part of the wall.)

4. Numerical results and discussion

As can be seen from the programming rules given above, we do not teleport the field back onto the source cells. This is because it turns out that field teleportation back onto the source walls leads to blowing-up of the solution since the algorithm gets caught in a feedback loop. Therefore, we teleport the copied fields one cell beyond where they were collected and compensate for this one cell shift by storing the fields one step in time in the past. This means that the cancellation is not perfect, but it is very good (typically of the order of -20 dB, time domain average, per wall). To obtain deeper cancelation RBC walls can be cascaded one behind the other as described above. For the sake of clarity, this chapter is divided into three sections describing different numerical experiments.

4.1. "Anechoic-chamber" test

To demonstrate the difference between one- and two-walls of the RBC, we model a two-dimensional "anechoic chamber" in free space. A square 2D X–Y domain 200 by 200 cells in area was alternately surrounded with one or two RBC walls. A z-directed electric field is injected exactly in the center of the domain having a time dependence of the form:

$$\begin{cases} \text{pulse} = \sin^3(2\pi n/60), & 0 \leqslant n \leqslant 60, \\ \text{pulse} = 0, & n > 60, \end{cases}$$

For all the following examples $ds/cdt = 0.5$. The total energy within the domain (normalized to its maximum value) as a function of the time step n, for both cases, is shown in Fig. 3. The positions of the second (internal) RBC wall for each side are given in Table 2.

Fig. 3 shows that the one-wall RBC approximately gives -40 dB in total energy suppression per bounce (-50 dB for 2-walls). The stair-casing of the curves is caused by the subsequent bounces of the residual echo. However, there is no big difference in the residual energy for the late time. Notice, that gauging the performance this way measures the absorption in the time domain and not at any particular frequency.

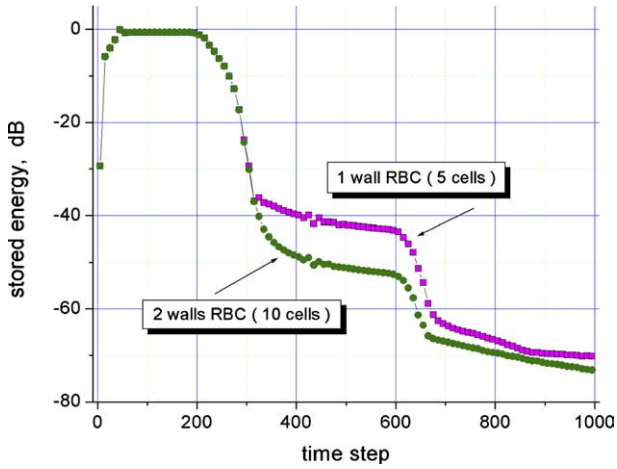

Fig. 3. Stored energy versus time step for 1-wall (squares) and 2-walls RBCs for the anechoic chamber modeling.

To illustrate the late-time stability of the proposed algorithm for a bipolar excitation (no dc content), a numerical comparison of the RBC and the unsplit PML for extremely long run times is considered. No special attempts have been made to optimize either RBC or PML in this testing configuration. The 2D-TE code with PML from Sullivan's book [15] has been employed "as is" with a soft signal injection. The unsplit PML (UPML) scheme employs a cubical law of conductivity. A comparison between 2-walls RBC and 10-cells UPML has been done for the same "anechoic chamber" configuration. The $ds/cdt = 0.5$ rule has been used for the cases. Fig. 4 shows the results. The proposed RBC absorbs outgoing waves much better than tested UPML up to one thousand time steps, giving −75 dB attenuation after a second echo reflection (−50 dB for the UPML). In the late time, there is no big difference in the residual field left in the room, between UPML and RBC. This suggests that this field is due purely to truncation noise. This simulation is an illustration of the adequacy of the $R = 0.99$ factor to prevent long-time instability for any bipolar symmetrical excitation. However, given that the recipe has integrator-like properties (albeit imperfect) from the wrong side of the boundary, a complete the study on the long term stability of the RBC will require further numerical experiments with pulses containing significant dc content.

It should be noted that the proposed multi-stack RBC algorithm consumes less computer time and memory than the UPML. A 6000 time steps anechoic chamber test run took 330 s for the RBC scheme and 583 for the UPML (and used 12 Mb memory versus 20 Mb for the UPML.) For our FDTD modeling, an ordinary Dual Athlon PC 1.5 GHz has been used (no special attempts, like parallel code execution were taken to give an advantage to either code).

Table 2
Locations of the RBC walls ($nx = 200$, $ny = 210$)

	H-update RBC loops	E-update RBC loops
Left wall	$H_y(3, j)$, $j = 1, \ldots, ny$	$E_z(2, j)$, $j = 1, \ldots, ny$
Right wall	$H_y(nx - 1, j)$, $j = 1, \ldots, ny$	$E_z(nx - 1, j)$, $j = 1, \ldots, ny$
Top wall	$H_x(i, ny - 1)$, $i = 1, \ldots, nx$	$E_z(i, ny - 1)$, $i = 1, \ldots, nx$
Bottom wall	$H_x(i, 3)$, $i = 1, \ldots, nx$	$E_z(i, 2)$, $i = 1, \ldots, nx$

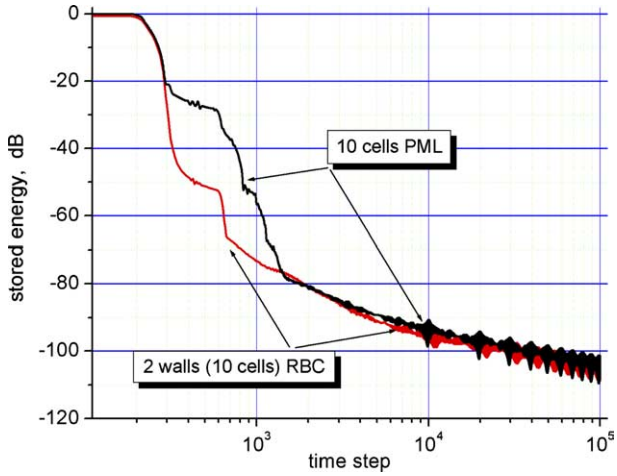

Fig. 4. Comparison between 10-cells UPML and 10-cells RBC performance for the abechoic chamber modeling.

4.2. Shallow-angle reflection test

Absorption performance for a wide range of incidence angles is still a subject of investigation and modeling for many researchers. Shallow angle incidence remains a big challenge for developing a good absorption layer, especially if it cuts through different materials. Simultaneous comparison of near-field and shallow angle absorption between the proposed RBC and the UPML can be obtained using the numerical experiment illustrated in Fig. 5. Again 2D-TE FDTD is used. A rectangular area (1050 by 700 cells) is terminated by the two-walls RBC and contains a point source, located either in the point S_r ($i = 700$, $j = 350$) or in the point S_m (700,30). Smooth injection of a continuous cylindrical wave $\sin(2\pi n/60)(n^2/(n_2 + 60))$ has been applied for the E_z component of the field. The measurement area is a rectangular region 590 by 40 cells located close to the source. (This corresponds to a period of 60 dt, or 30 cells per wavelength.)

For the first reference configuration (source is in the S_r point), the field in the measurement area is unaffected by the boundaries during the first 1200 time steps, since it takes about 1360 time steps for an echo to reach the measurement area after reflecting of the RBC boundary. Performing the windowed Fourier Transform for every cell in the measurement area and storing data as a two-dimensional E_z magnitude distribution we develop a reference or free-space field distribution. Then, moving the source and the test region toward the ABC layer (second configuration) introduces into the measurement area the signal reflected from the bottom absorbing boundary. Comparison between the first and second results measures the

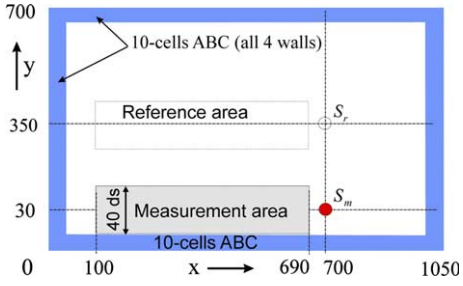

Fig. 5. Scheme of the numerical experiment S-initial source position, (b) the source is close to the ABC layer.

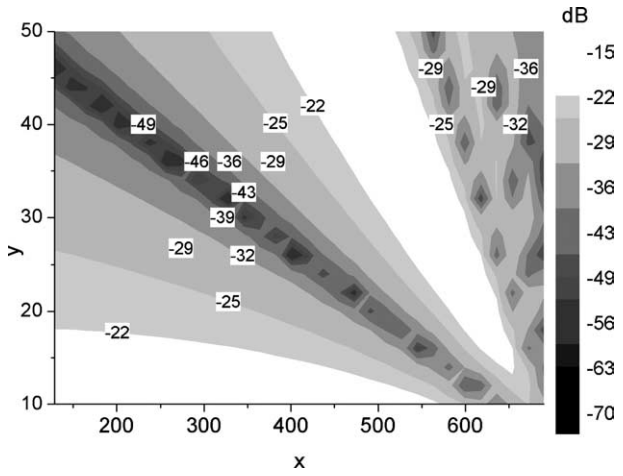

Fig. 6. The difference in the near-field magnitude introduced by 10-cells UPML over the measurement area (the reference's maximum magnitude is one unit). The source is at $x = 700$, $y = 50$.

quality of absorption over the wide range of incident angles represented by the measurement area (roughly from 30° to 88°).

Fig. 6 shows the error between the complex field magnitude $E_m(x, y)$ in the presence of the 10-cells PML and the reference distribution $E_r(x, y)$, calculated as $20\log(|E_r - E_m|)$. The tested UPML heavily perturbs the near field and strongly decreases the magnitude of the field for shallow angles of the incidence. The worst case error introduced by the UPML into the measurement is about −15 dB. Fig. 7 shows the results of the numerical experiment for the two-walls RBC. The near-field perturbation for the RBC case is about −30 dB and occurs only for very shallow incidence angles ($\theta_{inc} \geqslant 80°$).

For ease of illustration this and the following experiments were performed with harmonic sources and relatively high resolution (30 cells per wavelength). As is obvious from the RBC recipe, the attenuation occurs in real time in the time domain. In [13], the normal incidence reflection coefficient of a two-stack RBC

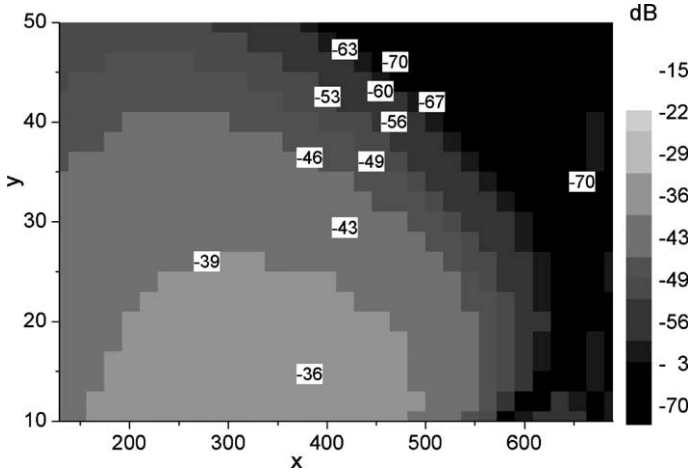

Fig. 7. The difference in the near-field magnitude introduced by 2 wall-RBC over the measurement area (the reference's maximum magnitude is one unit). The source is at $x = 700$, $y = 50$.

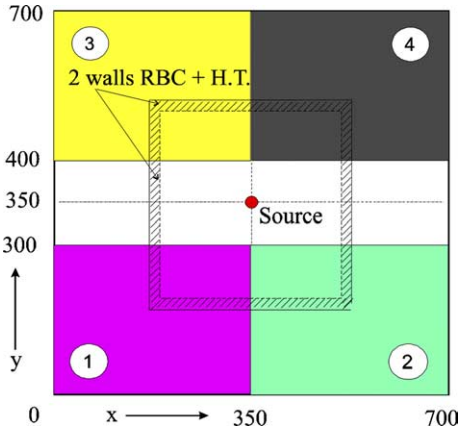

Fig. 8. Geometry of the test problem for RBC field termination in different materials.

terminated with a Huygen's wall is shown to saturate at −80 dB at very long wavelengths (because of the $R = 0.99$ limitation), then it rises gently to −60 dB around 90 cells per wavelength, −40 dB around 9 cells per wavelength and −20 dB at the grid cutoff.

4.3. RBC cutting trough inhomogeneous media

A more challenging problem for Absorbing Boundary Conditions is that of terminating an inhomogeneous domain. Fig. 8 shows a test geometry for illustrating RBC field termination in different materials. The square area (700 by 700 cells) is occupied by four different materials (numbered from 1 to 4) and a free-space center region. The point source is placed exactly in the center of the area. Similarly to the previous case, when the continuous wave source turns on, the cylindrical wave is generated and propagates outward from the center. At least 700 time steps pass before the wave sees any influence from the external boundaries. If we store the time history of the propagating wave in a smaller rectangular region (the tested area) and perform the windowed Fourier Transform, we will have a reference field distribution inside this zone.

However, if we introduce the RBC walls together with Huygens's termination around this tested area (shown as hatched border), the field inside the tested area will be corrupted somehow by reflections from the introduced ABC. Comparison between the RBC-terminated and reference field distribution gives the error introduced by the proposed RBC.

The frequency of the injected signal has been chosen as $f = 10$ GHz, that gives $\Delta t = 1.25$ ps and $\Delta s = 0.75$ mm. Table 3 gives the parameters of all materials used in this case.

Table 3
The parameters of materials

Material #	ε_r	σ_e (S/m)	μ_r	σ_m (Ω/m)
1	3	0.1	1	0
2	2	0.1	2	0.1
3	2	0	1	0
4	3	0	2	0.1

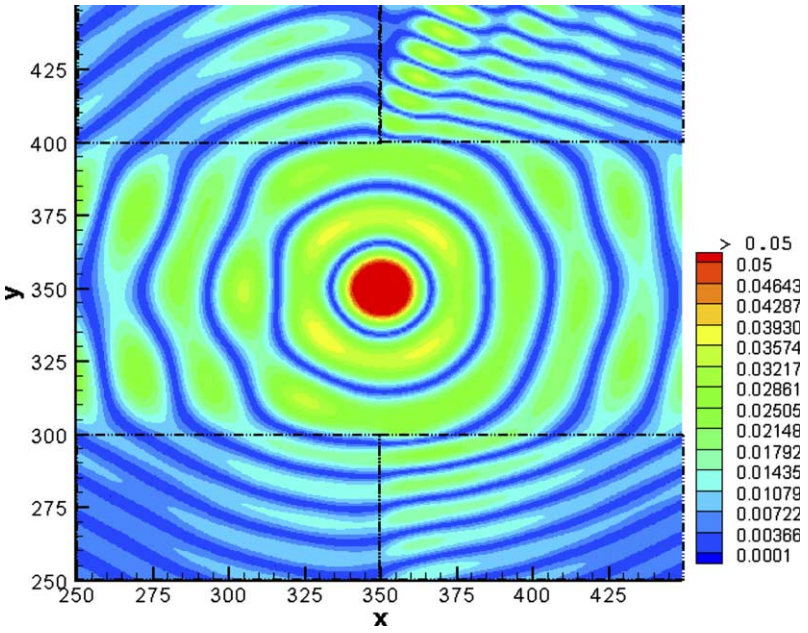

Fig. 9. The E_z component distribution (after the Fourier Transform) in the tested area.

Fig. 9 is the baseline, showing the reference E_z field distribution in the tested area. Since the maximum field magnitude in the source point is very strong compared to those in the surrounding materials, the color intensity corresponding to the strongest field is saturated. The material interfaces are shown as dashed lines.

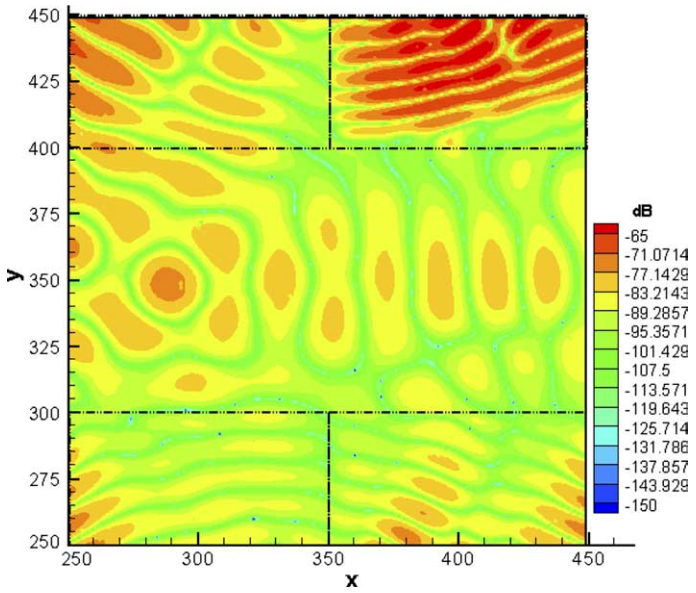

Fig. 10. The reflection from 2-walls RBC (introduced error) in the tested area in the case of multiple material boundaries.

Fig. 10 shows the spatial distribution of the signal reflected from the RBC after subtracting the baseline (that is, the introduced error). The reflection from the RBC which cuts through five different materials does not exceed −65 dB. The highest reflection occurs from the 4th material, which has the highest refractive index $n = \sqrt{\varepsilon_r \mu_r} \approx 2.45$ and where the ratio $n\Delta s/(c\Delta t)$ is much higher than the free space 0.5 value.

The results of Fig. 10 show that the proposed multi-stack RBC cuts transparently through all media. This is clear from the smooth way the contours of the residual scattered energy in Fig. 10 cross the material boundaries. There is no scattering source associated with any of the transitions from material to material. For the RBC, since the attenuation of the outgoing waves is created by exact FDTD copies of the incident waves, impedance matching occurs automatically. No special actions different from the regular FDTD updates have to be taken to update the field on the RBC, since the algorithm is independent of transverse variation of parameters along the RBC plane. No special treatment is required for corners since the individual RBC walls simply cut through each other transparently.

5. Conclusion

In this paper, the Field Teleportation principle, based on discrete equivalent currents, has been successfully applied for developing a new FDTD absorption boundary condition, called a multi-stack Radiation Boundary Condition (MS-RBC). It consists of one or more teleportation boundaries that create field cancellation by radiating forward a negative copy of the fields incident upon the boundary, and a grid termination condition such as a Huygens's wall. Because the RBC uses the discrete curl of FDTD and the fields created inside the FDTD space itself, it matches the FDTD grid in all respects (including grid dispersion, material dispersion, and propagation anisotropy). Therefore the proposed MS-RBC provides a transparent, and innocuous boundary for the termination of the FDTD grid. The only reflection from the teleportation boundary is truncation noise, as is common with the FDTD grid itself, because Schelkunoff's equivalent currents do not radiate backwards. Thus the only source of reflection is the damped reflection from the Huygens's wall at the end of the grid. The spatio-temporal asymmetry of the recipe prevents this reflection from being re-amplified as it travels backwards through the RBCs, yielding a net absorption of the order of −80 dB for a stack of two RBC boundaries, up to shallow angles. The MS-RBC is near-field innocuous because the teleportation scheme does not cause any reaction on the source field, even when that source field is a reactive near-field or an evanescent surface wave. Good shallow angle absorption has been demonstrated. In addition, the MS-RBC is straightforward to program requiring no selection of a conductivity gradient and no special treatment of corners. Finally, it consumes less computational resources than the unsplit PML. We anticipate that the MS-RBC technique can be used independently as well as together with other FDTD ABCs strongly enhancing their performance.

References

[1] M.E. Watts, R.E. Díaz, Perfect Plane-Wave Injection into a finite FDTD domain through Teleportation of Fields, Electromagnetics 23 (2003) 187–201.
[2] C.J. Railton, E.M. Daniel, A comparison of the properties of radiating boundary conditions in the FDTD method for finite discretisation and non-planar waves, IEEE Trans. Antennas Propagat. 42 (2) (1994) 276–281.
[3] B. Engquist, A. Majda, Radiation boundary conditions for the numerical simulation of waves, Math. Comput. 31 (1977) 629–651.
[4] G. Mur, Absorbing boundary conditions for the finite-difference approximation of the time-domain electromagnetic-field equations, IEEE Trans. Electromagn. Compat. 23 (1981) 377–382.
[5] R.L. Higdon, Numerical absorbing boundary conditions for the wave equation, Math. Comp. 49 (1987) 65–91.
[6] J. Fang, K.K. Mei, A super-absorbing boundary algorithm for solving electromagnetic problems by time-domain finite-difference method, Antennas and Propagation Society Int. Symp., AP-S. Digest 2 (1988) 472–475.

[7] T. Deveze, F. Clerc, W. Tabbara, Second order pseudo-transparent boundary equations for FDTD method, Antennas and Propagation Society Int. Symp., AP-S. Digest. (4) (1990) 1624–1627.
[8] J.P. Berenger, A perfectly matched layer for the absorption of electromagnetic waves, J. Comp. Phys. (114) (1994) 185–200.
[9] C. Liao, L. Meng, D. Yang, X. Zhong, Analysis of the numerical error for the time domain Mei absorbing boundary condition, in: Proc. of APMC 2001, Taipei, Taiwan, pp. 839–842.
[10] Y.W. Liu, C. Liao, K. Lan, K.K. Mei, K.N. Yung, Absorbing boundary conditions for measured equation of invariance in time domain, Antennas and Propagation Society Int. Symp. (2) (1998) 1050–1053.
[11] A.A. Ergin, B. Shanker, E. Michielssen, Accuracy and efficiency of PWTD enhanced exact radiation boundary conditions in FDTD simulations, IEEE Antennas and Propagation Society Int. Symp. 0 (3) (2000) 1354–1357.
[12] Jean-Luc Vay, Anew absorbing layer boundary condition for the wave equation, J. Comp. Phys. 165 (2) (2000) 511–521.
[13] R.E. Diaz, I. Scherbatko, A Simple Stackable Re-Radiating Boundary Condition (rRBC) for FDTD, IEEE Antennas and Propagation Magazine 46 (1) (2004) 124–130.
[14] C.A. Balanis, Advanced Engineering Electromagnetics, Wiley, New York, 1989.
[15] D.M. Sullivan, Electromagnetic Simulation Using the FDTD Method, IEEE Press Series on RF and Microwave Technology, 2000.